Anomalous intracellular transport phases depend on cytoskeletal network features

Bryan Maelfeyt,[1] S. M. Ali Tabei,[2] and Ajay Gopinathan[1,*]
[1]*Department of Physics, University of California Merced, Merced California, USA*
[2]*Department of Physics, University of Northern Iowa, Cedar Falls Iowa, USA*

(Received 8 November 2018; revised manuscript received 9 March 2019; published 7 June 2019)

Intracellular transport in eukaryotic cells consists of phases of passive, diffusion-based transport and active, motor-driven transport along filaments that make up the cell's cytoskeleton. The interplay between superdiffusive transport along cytoskeletal filaments and the anomalous nature of subdiffusion in the bulk can lead to novel effects in transport behavior at the cellular scale. Here we develop a computational model of the process with cargo being ballistically transported along explicitly modeled cytoskeletal filament networks and passively transported in the cytoplasm by a subdiffusive continuous-time random walk (CTRW). We show that, over a physiologically relevant range of filament lengths and numbers, the network introduces a filament-length sensitive superdiffusive phase at early times which crosses over to a phase where the CTRW is dominant and produces subdiffusion at late times. We apply our approach to the problem of insulin secretion from cells and show that the superdiffusive phase introduced by the filament network manifests as a peak in the secretion at early times followed by an extended sustained release phase that is dominated by the CTRW process at late times. Our results are consistent with *in vivo* observations of insulin transport in healthy cells and shed light on the potential for the cell to tune functionally important transport phases by altering its cytoskeletal network.

DOI: 10.1103/PhysRevE.99.062404

I. INTRODUCTION

Motor-driven intracellular transport is an important process in eukaryotic cells [1–3] that is responsible for the delivery of a variety of material such as carbohydrates, nucleic acids, lipids, proteins [4], and even entire organelles like mitochondria [5] to target destinations in various places throughout the cell. This process comprises two phases, an active, molecular motor-driven phase and a passive, diffusive transport phase. In the active phase, cargos, typically material carried in vesicles, are pulled by ATP-powered molecular motors that walk in a hand-over-hand style of motion along a complex cytoskeletal meshlike network composed of actin filaments and microtubules [1]. The molecular motors that carry cargos belong to one of three classes. Myosin motors, which typically move towards the (+) end of actin filaments, kinesin motors which move toward the (+) end of microtubules, and dynein motors which move in the (−) direction along microtubules [6,7]. Actin and microtubule networks can form a variety of morphologies depending on cell type and function, ranging from random networks within the cell to oriented stress fibers for actin [8], and from radially oriented filaments to long parallel bundles for microtubules [9]. Motors, and hence the cargos they're carrying, also unbind from the filaments in a stochastic manner, whereupon they undergo passive diffusion in the cytosol till they bind to a filament again. Cargos thus alternatively bind and unbind from filaments in the network, undergoing passive and active transport, until they reach their target destination [10]. This process has been studied extensively from the perspective of the individual molecular motors that carry cargo [11] as well as the role of teams of motors in accomplishing transport [12–17]. Some of the related complexities that have attracted interest include motor-defect interactions on filaments [18], the existence of obstacles and roadblocks [19–21], and traffic jams on filaments [12,19].

In the past few years, however, there has been growing interest in how the global architecture and properties of the cytoskeletal network influence transport. Network features, characterized by the density, lengths, locations, orientations, and connectivity of filaments [22–24] as well as defects, posttranslational modifications, and blockades along them [1,25,26], likely influence intracellular transport in much the same way that road connectivity and conditions are critical determinants of vehicular traffic. For example, it has been shown that particular filament arrangements can result in "traps" near the nucleus that result in highly variable transport times, while other architectures result in rapid directed transport [22]. These results indicate the importance of the network architecture, but it is worth noting that the overall transport process is dependent on diffusion in the passive phase as well. While previous studies [22] assumed that the passive diffusive was characterized by normal Brownian diffusion, in the context of the crowded cytoplasm [27], diffusion is known to be anomalous [28]. Experiments involving measurements of diffusion of cargo after filament depolymerization in both extracts [28] and cells [4] have shown anomalously subdiffusive behavior. In fact, anomalous diffusion can be used to describe the entire intracellular transport process. The active transport phase is superdiffusive while anomalous subdiffusion is considered to be a characteristic of the passive transport phase within the bulk cytoplasm [2].

In this paper, we explore how the interplay between superdiffusive transport, provided by explicitly modeled

*agopinathan@ucmerced.edu

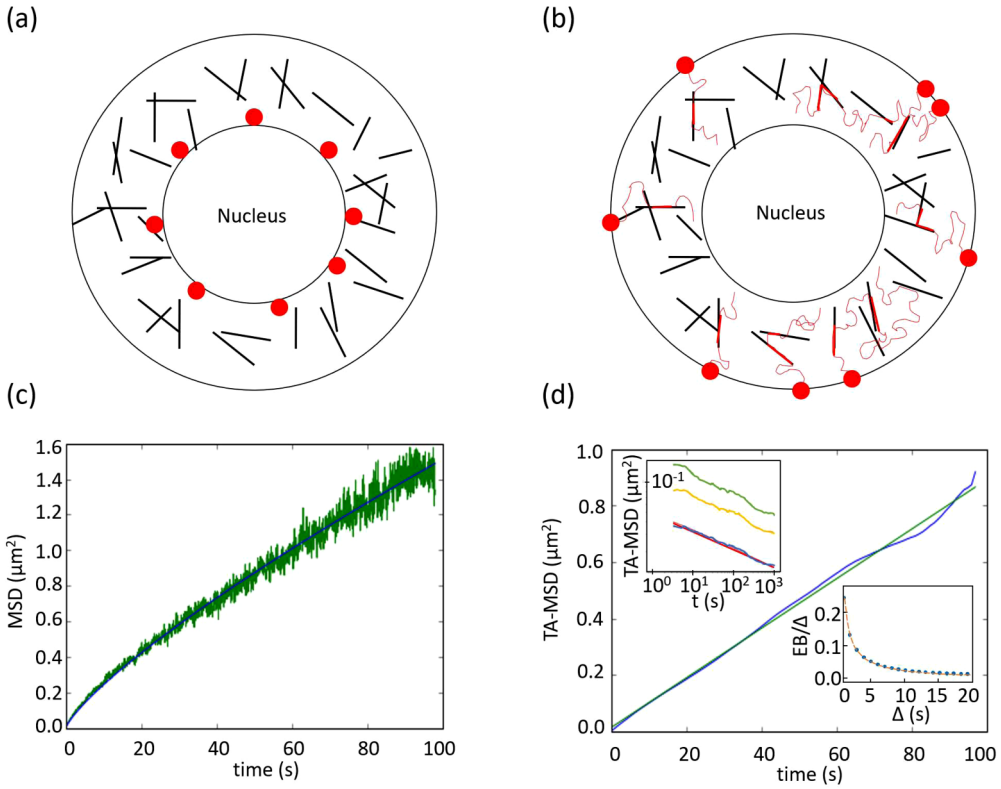

FIG. 1. (a) The initial state of the system. Cargos [shown as (red) circles] start near the nucleus. Randomly placed filaments (straight lines) model the cytoskeleton. Each filament has a fixed polarization. (b) The final state of the simulation. Cargos alternate between passive and active phases of transport until they reach the outer cell membrane. Individual trajectories are denoted by thin (red) curves traced out by the cargos. (c) The ensemble-average MSD for a system of 1000 cargos, with no filaments present (CTRW only). The smooth (blue) curve going through the data is a power-law fit with an exponent $\alpha = 0.8$. (d) TA-MSD for the same system for a constant measuring time, t, as a function of a sliding time window Δ. Inset, upper left shows the TA-MSD for constant time windows (1 s, 2 s, and 3 s, from top to bottom), as a function of measuring time. Inset, lower right, shows the ergodicity-breaking parameter plotted as EB/Δ as a function of Δ (dashed line shows $1/\Delta$).

cytoskeletal filaments, and the anomalous nature of subdiffusion in the bulk can lead to novel effects in transport behavior at the cellular scale. In particular, we are interested in how the geometric properties of the cytoskeletal network dictated by the lengths and density of the constituent filaments influence transport in the presence of anomalous subdiffusive transport in the bulk cytoplasm, and especially whether they can be tuned to access different transport phases. Anomalous diffusion can generally be described by two prevailing models, fractional Brownian motion (FBM) [29], which is an ergodic process, and continuous-time random walk (CTRW) [30], which is not. In the context of intracellular transport, CTRW has been shown to describe bulk diffusion when filaments are shortened *in vivo* [4,28,31] as well as in the presence of cargo interactions with filaments [31] and vortices and cycling behavior near actin filament intersections in the case of multiple molecular motors [32]. It has also been observed that diffusive cytosolic transport is best explained by a CTRW, while filament transport is best represented by FBM [28]. While different mechanisms have been proposed in these papers, their relative contributions to the observed CTRW behavior is not clear yet and is beyond the scope of this paper. The goal of our paper is to show how the observed CTRW for passive cargo diffusion in conjunction with active transport on cytoskeleton structures influence the overall transport properties. Since we use explicit filament networks, we need only to account for anomalous subdiffusion in the bulk in our model, which we therefore do, using CTRW.

Given our focus on understanding the basic physics of the interplay between superdiffusive network transport and subdiffusive cytoplasmic transport, we choose to consider only the simplest geometries for the cytoplasmic boundaries and cytoskeletal networks. Our model, introduced in Sec. II, consists of a circular cell with a concentric circular nucleus and a randomly oriented filament network between the nuclear and cellular membranes (see Fig. 1). In this case, the geometric properties of the cytoskeletal network are dictated by the lengths and density of the constituent filaments. We simulate the transport of cargos, starting at the nucleus, in the center of the cell, and alternating between ballistic transport along the filaments and subdiffusive transport in the bulk, till they reach their target destination; the outer cell membrane. For the sake of simplicity, and, in order to focus only on relevant parameters such as filament length, concentration, and dwell time statistics of anomalous diffusion, we neglect the elasticity of the filaments [33], viscoelastic interactions between cargos, motors, and the network [34], confinement effects [35,36], and scenarios involving cargos carried by multiple motors [37] (we consider only single-motor active transport). As the simulation unfolds, we measure mean-squared

displacements (MSDs) as a function of time and the distributions of first-passage times (FPTDs) to get to the destination for cargos over multiple filament networks for varying network parameters (filament length and concentration). Because we explicitly model the filament geometry, we are also able to compute the variance in these measurements across multiple network realizations with the same parameters. We should emphasize here that we focus on quantities like the MSD, the time-averaged MSD, and first-passage time distributions because they give us physiologically relevant information like overall transit times and also because they are readily and typically measured quantities in microscopy experiments. Therefore this approach allows us to reveal the signatures of underlying anomalous processes in macroscopic and averaged observables that are readily experimentally accessible.

To begin, in Sec. III we consider the case of pure cytosplasmic subdiffusion in the absence of filaments. We verify that our implementation of CTRW produces the desired behavior for both ensemble-averaged and time-averaged MSDs. In Sec. IV we consider the addition of a network of filaments to the system. We show, over a physiologically relevant range of filament lengths and numbers, that the network introduces a superdiffusive phase at early times which crosses over to a phase where the CTRW is dominant and produces subdiffusion at late times. We also show that the superdiffusive phase is most sensitive to filament length. In Sec. V we apply our simulation approach to the problem of insulin secretion from pancreatic cells, which is characterized, in healthy cells, by a quick release of a large fraction of granules followed by a low but sustained rate of release at late times after glucose stimulation [38]. We show that the superdiffusive phase introduced by the filament network manifests as a peak in the secretion at early times followed by an extended sustained release phase that is dominated by the CTRW process at late times. Our results are consistent with *in vivo* observations of insulin transport and shed light on the potential for the cell to tune transport phases by altering its cytoskeletal network.

II. METHODS

We build on previous work [22] in which simulations of cargos alternate between phases of ballistic motion along filaments (corresponding to active transport) and random walk phases resulting in Brownian motion or normal diffusion in the bulk (corresponding to passive transport). For our simulations, we consider a model eukaryotic cell consisting of a nucleus, cell membrane, and filaments that make up the cytoskeleton. We use biologically realistic parameters for the various processes involved [22] (see Ref. [39]) and implement all of our simulations in two dimensions, in order to better compare our results with experiments, where processes are typically observed in a two-dimensional (2D) plane. The cell, then, is represented by a 2D disk with a radius of 10 μm, while the nucleus has a radius of 5 μm. Filaments are straight lines with random locations and orientations (see Refs. [22] and [39] for more details on network generation). Cargos have a radius of 100 nm and bind to filaments with a rate of $k_{on} = 5\ \mathrm{s}^{-1}$, and unbind from filaments at a rate $k_{\mathrm{off}} = 1\ \mathrm{s}^{-1}$. The cargo radius influences only the diffusion constant and the range of interaction of cargos. Cargos begin near the nucleus [Fig. 1(a)] and undergo transport until they reach the cell membrane [Fig. 1(b)] while alternating between phases on and off the filament network. Off the network, the diffusion constant (in the case of normal diffusion) is $D = 0.051\ \mu\mathrm{m}^2/\mathrm{s}$, and while traveling on the network, cargos move at a speed of $v = 1\ \mu\mathrm{m/s}$.

In this work, we extend the previous model [22] by accounting for the fact that cargos can undergo anomalous subdiffusion instead of regular diffusion during the passive phase. A signature of anomalous diffusion is that the cargos have a MSD that scales as

$$\langle r^2(t)\rangle \sim t^{\alpha} \tag{1}$$

with $0 < \alpha < 1$ indicating subdiffusion. In order to incorporate anomalous diffusion in our simulations, we have cargos perform a CTRW during the passive transport phase. To implement this, we select a waiting or dwell time between successive random walk steps, from the distribution

$$\psi(t) = \begin{cases} 0 & \text{if } t < 1 \\ \alpha t^{-\alpha-1} & \text{if } t \geqslant 1 \end{cases} \tag{2}$$

with $0 < \alpha < 1$. After waiting for the selected time, the cargo moves a distance of 0.1 μm, with the maximum cargo movement speed being set by the diffusion constant. Experiments with cargo in cell extracts [28] have shown that, in the presence of microtubules, cargos move with a measured α of about 1.4–1.5, but when the filaments are depolymerized, α values between 0.65 and 0.98 were observed. These results seem to indicate that diffusion in the absence of any filaments, due to the bulk alone, is subdiffusive with an exponent of about 0.8. This value is also consistent with the subdiffusive exponent observed for insulin granules in pancreatic cells that had been treated by vinblastine to depolymerize filaments [4]. Based on these and other [31] similar results, we use $\alpha = 0.8$ in most of our simulations, unless otherwise specified.

III. VALIDATING MSD SCALING AND AGING DUE TO CTRW

We begin our simulations with a test of our system in the absence of any filaments. Here cargos begin near the nucleus and undergo purely passive transport (CTRW only) until they reach the outer membrane. For purely CTRW transport with a distribution of wait times defined by Eq. (2), we expect the MSD to scale according to Eq. (1). Figure 1(c) shows the ensemble-averaged MSD from our simulations, which agrees very well with the expected power-law scaling with an exponent of 0.8.

Since CTRW is a nonergodic process, we also analyze time-average mean-squared displacement (TA-MSD) data. By definition, this value is given by [40]

$$\overline{\delta^2}(\Delta, t) = \frac{\int_0^{t-\Delta} [x(t'+\Delta) - x(t')]^2\, dt'}{t - \Delta}, \tag{3}$$

where Δ is the sliding time window (time between measurements) and t is the total measuring time. In the limit where $\Delta \ll t$, averaging over many cargos yields

$$\langle\overline{\delta^2}\rangle \sim \frac{\Delta}{t^{1-\alpha}}. \tag{4}$$

From Fig. 1(d) (main), we see that the measured TA-MSD increases linearly with Δ, as expected. In Fig. 1(d) (upper-left inset), we plot scaling of the TA-MSD from simulations with measuring time t for different values of $\Delta = 1$ s, 2 s, 3 s. We again recover the expected scaling behavior, $t^{1-\alpha}$. Finally, we also plot the measured ergodicity-breaking (EB) parameter,

$$\mathrm{EB} = \frac{\langle(\overline{\delta^2})^2\rangle - \langle\overline{\delta^2}\rangle^2}{\langle\overline{\delta^2}\rangle^2}, \tag{5}$$

in Fig. 1(d) (lower-right inset) as EB/Δ, which scales as $\sim 1/\Delta$ as expected for CTRW [4], signifying convergence of EB to a nonzero constant value, another characteristic feature of CTRW. Taken together, these results indicate that our CTRW model implementation is effective in producing anomalous subdiffusion with the desired exponent.

IV. ADDING FILAMENTS INTRODUCES A SUPERDIFFUSIVE PHASE

Having validated and created a baseline for the MSD scaling in the subdiffusive passive phase, we now consider the addition of filaments, creating a cytoskeletal network. We add to the network 100, 200, 300, 400, and 500 filaments, with lengths of 1, 2, 3, 4, and 5 μm (details of network generation are in Refs. [22] and [39]; the range of filament numbers and lengths are consistent with reasonable *in vivo* values [22]). The most notable difference is observed in the ensemble-average MSD. We can see in Fig. 2(a) that, in contrast to the case with no filaments present, the MSD in

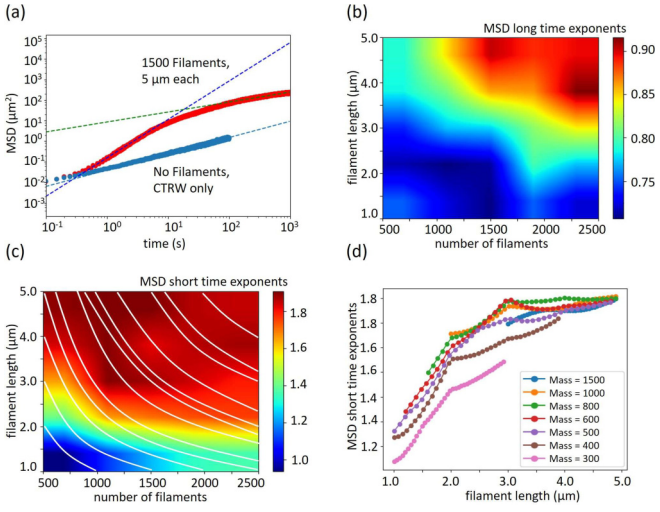

FIG. 2. (a) A log-log plot of an ensemble-average MSD in the presence of filaments (1500 filaments, 5 μm each) compared to MSD for CTRW only [lower set of data points (blue symbols)]. Dashed lines show fits to different power-law behaviors for short and long times for the MSD data with filaments and over the entire time range for the control CTRW-only case. The measured long- (b) and short-time (c) power-law exponents as a function of filament length and number. In panel (c) lines of constant mass are in white. (d) MSD short-time exponents as a function of filament length for different total filament masses. Averaging is over $N = 10\,000$ cargo in all cases. Error in the measured exponents due to fitting is less than 6% over the parameter range explored.

the presence of filaments shows different scaling behaviors in different time regimes. Fitting the MSD in the two time regimes, we can see that the short-time slope is larger than 1 (indicating superdiffusion with an MSD scaling exponent larger than 1) and is distinctly larger than the long-time slope, which is below 1 (indicating subdiffusion). Thus at early times, it appears that the MSD is dominated by movement along the filaments, giving rise to superdiffusion. At later times, past some transition time (set by the typical timescale for which a cargo walks on a filament before detaching, between 1 and 10 s), we can see a crossover to CTRW-dominated behavior, as suggested by comparing the slope of this second regime with the slope of the CTRW-only data. To understand how these different exponents depend on the network parameters, we plot the MSD scaling exponents in the long-time [Fig. 2(b)] and the short-time [Fig. 2(c)] regimes as a function of number and lengths of the filaments. Consistent with the picture that the long-time dynamics are controlled by CTRW, the long-time exponents are all close to 0.8 and fairly insensitive to filament density and number, except at the very highest network masses, where the signature of the short-time superdiffusive phase begins to show. Note that the exponent appears to go below 0.8 at low densities because of confinement effects from the boundary, and, as expected, this effect diminishes with increasing cell radius (see Ref. [39]). Not surprisingly, the network parameters have the greatest effect on the MSD at shorter times, where the slope is greatest. The short-time exponent changes all the way from 1 (or diffusive) at the lowest network masses to almost ballistic ($\sim$1.8) at high network masses. To examine the relative importance of filament length and density, we consider curves of constant mass [white lines in Fig. 2(c)], where filament mass is defined as the number of filaments multiplied by the length of each filament. In Fig. 2(d) we plot the short-time MSD exponent as a function of filament length for different network masses [corresponding to the lines in Fig. 2(c)]. We see from the rough collapse of the curves that the short-time exponent shows very modest increases with greater mass at fixed filament length but is much more sensitive to the filament length for constant mass. This indicates that it is the filament length, not the total mass of the filaments, that is an important factor in driving the MSD at short times.

We now look more closely at the long-time behavior to understand how it is controlled by the CTRW. Figure 3(a) plots the MSD for values of α from 0.2 to 1 in the presence of 1500 filaments of length 5 μm. We can see the effect of the dwell time distribution on the MSD in the long-time regime [Fig. 3(a)]. Whereas the MSD is controlled by the filament network at early times and is insensitive to α, decreasing α leads to a decrease in the MSD at late times. Because we are interested in how the geometry of the network itself affects MSD, we next consider how the MSD varies across different network realizations. Figure 3(b) plots the MSD for five different networks, each with 300 filaments of length, 5 μm. We immediately see that any difference between them is within the intrinsic variance on each network due to the CTRW, suggesting that the variance due to the dwell time distribution dominates over network geometry effects. To quantify this further, we simulate the transport of 100 cargos over 100 networks and calculate the MSD at 10 s and 100 s

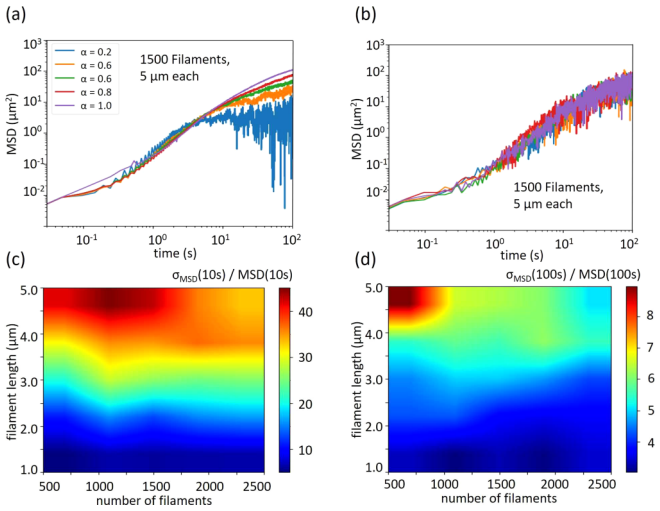

FIG. 3. (a) Ensemble-average MSD as a function of time for different values of α ($N = 100$ cargo) (b) MSD as a function of time for 100 cargos over five different networks at fixed $\alpha = 0.8$. Normalized standard deviation of MSD (averaged over 100 cargo and 100 different networks) at 10 s (c) and 100 s (d) as a function of filament length and number.

and track its variance at those times. Figures 3(c) and 3(d) show the standard deviations of the MSD at 10 s and 100 s (normalized by the mean MSD at those times), respectively, for different filament lengths and numbers. The normalized standard deviation increases with increasing filament length and decreasing numbers of filaments, with the effect being much more pronounced at early times when the network geometry is influential.

V. TUNING TRANSPORT PHASES USING NETWORK PARAMETERS

Of particular interest due to its relevance to real biological processes such a secretion and exocytosis is the time taken to transport cargo to the peripheral cell membrane. We can quantify this transport by measuring the time that it takes for cargo to first reach the outer membrane and constructing a first-passage time distribution (FPTD) from these times. Such FPTDs can have distinctive features that arise from the underlying transport processes. For example, it has been shown that insulin secretion in healthy pancreatic cells, where insulin-containing vesicles are transported to the membrane and secreted outside of the cell [4], is characterized by a distinctly "biphasic" FPTD, consisting of an initial spike, followed by a long, sustained release of insulin [38]. In a recent model [4] used to explain this process, insulin granules move throughout the cell through a combination of FBM and CTRW until they reach some distance a from a fast-releasing hot spot on the cell membrane, where the particles move only via FBM [38,41]. As the parameter a is increased, there is an initial peak of insulin flux followed by a more stable phase, giving the biphasic behavior seen in experimental observations. While the distance a is meant to model a region with no trapping, it is not clear what the physical cytoskeletal architecture would be corresponding to this parameter. While the insulin secretion process as a whole is complex involving many signals, regulatory proteins, fusion proteins, and motor proteins such as myosins and kinesins [38], *in vivo* observations suggest that the cytoskeletal network has an important part to play in this process and, in particular, that depolymerization and rearrangement of actin filaments seen during glucose stimulation is one of the key regulators [38,42,43]. Here we consider the network filaments explicitly and are therefore able to directly examine the result of filament depolymerization in isolation. The exact features of the secretion profile depend on the parameters and assumptions about the initial distribution of insulin granules. Rather than trying to replicate that, we focus on two main features observed in the biphasic secretion: fast secretion upon stimulation and sustained slow secretion, at later times. We use pure CTRW to represent anomalous diffusion in the bulk, and, instead of the parameter a, we vary, as in the case of our MSD analysis, explicit filament length and number. We monitor insulin flux out of the cell by making FPTD measurements for different network parameters.

Figure 4(a) shows FPTDs as a function of time for different filament lengths with a constant filament number of 300. It should be noted that we calculated the FPTD by binning the first-passage times of cargo (starting from a random position with a linearly decreasing probability with distance from the center) when they reached the membrane into 1 s time intervals bins. Our simulations have 100 cargos across 100 networks, which makes a total of 10^4 cargos. While the bins go out to 10^6 s, in Fig. 4(a) the FPTD plots are cut off at 1000 s. We notice that at the shortest filament lengths, the FPTD appears to have no peak. The first phase, the initial spike, is apparent only at a filament length of 3 μm and beyond. Thus the filament length clearly tunes this phase that occurs at early times. This is also consistent with our picture, from the previous section, that the early-time dynamics are controlled by filament length. Interestingly, it appears that all curves also show a sustained release at late times signified by the long tail. Our results from the previous section suggest that this second phase at late times is likely a power-law decay determined by the value of α. To examine this possibility, we focus on the FPTD behavior at late times. Figure 4(b) displays a log-log plot of FPTD as a function of time for a network with 300 filaments with a length of 5 μm each, but for different values of α. The larger the value of α, the steeper the decay, until in the case of $\alpha = 1$, the decay is qualitatively different and becomes exponential. To test whether this second phase can be tuned by the network geometry, we examine, in Fig. 4(c), the FPTD power-law exponent in the second, decaying, transport phase as a function of the filament length and number. We see that the exponent increases with network mass with a more sensitive dependence on filament length. The increase in the exponent is quite significant, from 0.2 to 1.2 in the range of filament parameters studied, indicating that, even though we are looking at relatively late times, the filament network can be used to tune the behavior in that phase too. To analyze this further, we plot, in Fig. 4(d), the FPTD decay exponent as a function of filament length for several different total filament masses. We see a separation between different mass curves indicating a dependence on the total mass as well as the filament length, with increases in both leading to a larger

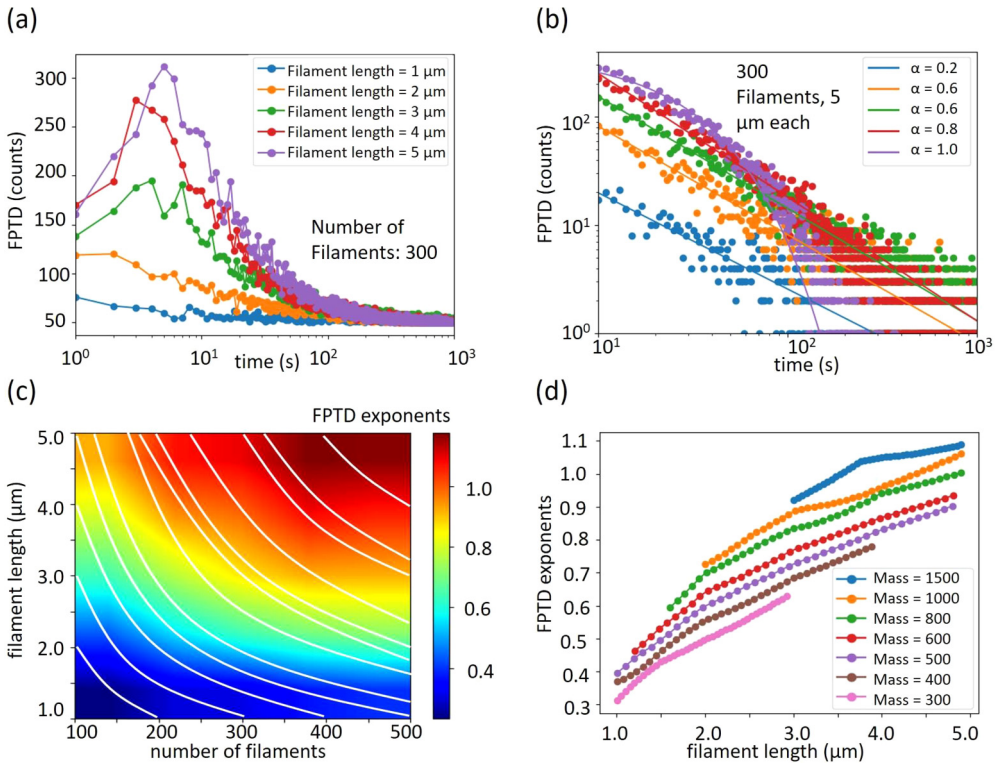

FIG. 4. (a) FPTDs for networks comprising 300 filaments, with varying lengths. (b) The second phase of the FPTD for different values of α. (c) Strength of FPTD decay as a function of filament length and number. Lines of constant mass are in white. (d) FPTD decay exponent as a function of filament length for different filament masses. FPTDs are for 100 cargo over 100 different networks. Error in measured exponents due to fitting is less than 6% over the parameter range explored.

exponent indicating a steeper decay, i.e., a curtailment of the sustained release phase.

Finally, we note that prior work on transport over explicit filament networks in a normally diffusive bulk produced trapping regions that significantly impacted the MFPTs [22] and also produced a significant variance in MFPT from network to network. To examine whether a similar effect occurs in the presence of cytoplasmic subdiffusion, we measured the MFPT from the FPTDs generated. Figure 5(a) shows the MFPT (μ) as a function of filament number and length, while Fig. 5(b) shows the dependence on filament length for fixed filament mass. Here μ denotes the average MFPT over all of the network configurations, as each network has its own associated MFPT. As expected, the MFPT decreases with increasing filament mass and filament length, indicating that filaments provide a superdiffusive boost to transport. To examine the effects of filament geometry on transport, we calculate how the MFPT varies across multiple networks. We first calculated the standard deviation for 400 cargo first-passage times on one network and then averaged them across 100 different networks to obtain the network-averaged standard deviation, μ_σ. Figure 5(c) shows μ_σ as a function of filament length and number. We notice that the variance decreases with increasing filament mass indicating that the superdiffusive phase introduced by the filaments works to counteract the variance from the CTRW in the bulk. Also of interest are the rather large values of the normalized average standard deviation [Fig. 5(d)], which is the network-averaged standard deviation divided by the MFPT obtained at each particular set of filament parameters. This means that any MFPT variation across networks is dominated by the randomness of the CTRW, which overcomes any variations caused by trapping regions due to changes in filament orientation. It is the variance μ_σ that gives rise to the sustained release phase, and thus, we see again that a decrease in the filament network mass results in increasing μ_σ and hence an increased sustained release.

VI. DISCUSSION AND CONCLUSION

In our studies, we have shown that motor-driven transport along filaments is most dominant at early times, as we find in our MSD calculations, where it is apparent that cargos move via superdiffusion. As we change network parameters, namely, the filament length and filament number, we can tune this superdiffusive behavior. Increasing the net filament mass increases the superdiffusive exponent speeding up the transport process, and for networks with the same mass, those with longer filaments facilitate even faster transport. The superdiffusion we see in the presence of filaments and the subdiffusion that begins to manifest as filament mass is decreased is consistent with the results found in Ref. [28], where α was measured to be about 1.5 in extract, but when the filaments are depolymerized, α decreased to between 0.65 and 0.98. In our simulations, we achieve [Fig. 2(c)] an α value of around 1.5 at a filament length between 2 μm and 3 μm. As we shorten our filaments, the short-time exponent drops and transport turns over to the late-time regime where CTRW

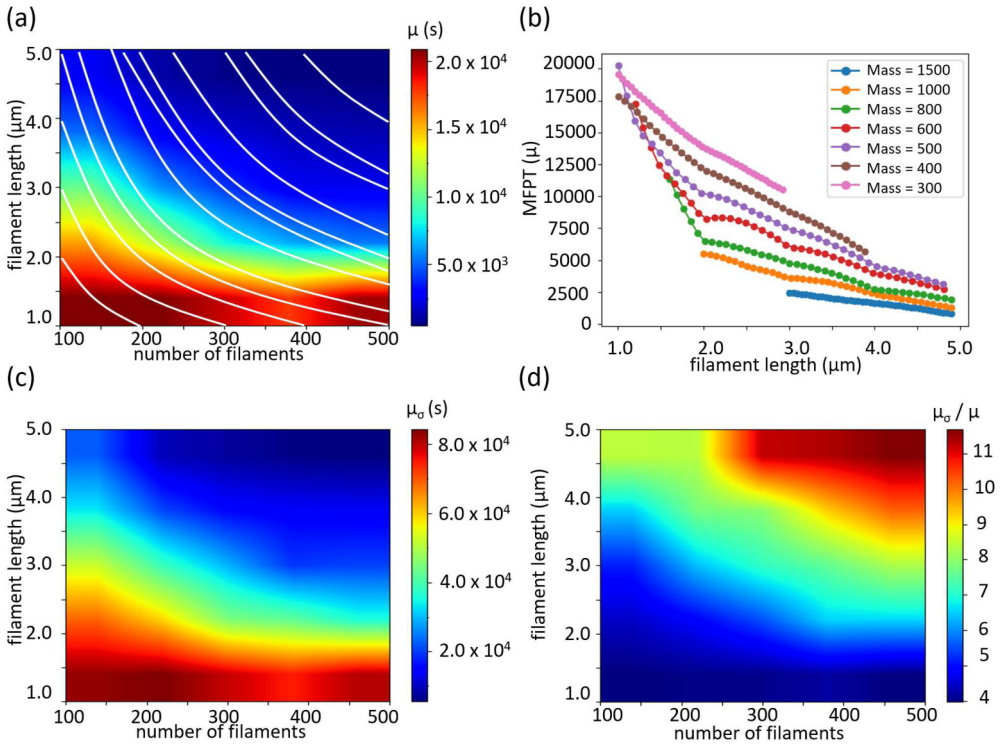

FIG. 5. (a) MFPT as a function of filament length and number with lines of constant mass in white. (b) MFPT as a function of filament length for different filament masses. Network-averaged MFPT standard deviation (c) and normalized average standard deviation (d) as a function of filament length and number. Averaging is over 400 cargo and 100 different networks.

dominates with an α of about 0.8 in the absence of filaments. It is to be noted that this value of α is also consistent with the results from insulin granule subdiffusion in cells treated with vinblastine (a microtubule depolymerizing agent) [4]. There they found that the correlated component of the walk (FBM), was limited to very early times ($\lesssim 10$ s) and that the process was mostly dominated by CTRW with an $\alpha = 0.8$. It is also interesting to note that their measurements of the TA-MSD exponent overall (in the absence of vinblastine) had a wide spread from subdiffusive to superdiffusive. Our results suggest that, in any such experiment, one could potentially observe a transition from a superdiffusive to a subdiffusive phase as a function of time, or even spatial location, if the network structure is heterogeneous. Thus our simulations of transport over explicit networks coupled to subdiffusion (CTRW) in the bulk highlight regimes where one or the other phase is dominant and quantitatively explains experimentally observed features.

While the role of the cytoskeleton in insulin secretion has not yet been fully understood [38], it is clear that both the cortical actin and microtubule networks are important for the process. It is also clear that there is certainly a reorganization of F-actin upon glucose stimulation that plays a key role. There has been debate about whether the reorganization acts as a removal of a barrier for the granules or a release of trapped granules and how that fits in with results that indicate myosin-powered motility of the granules along F-actin is also important. In our examination of insulin transport, we found that filament length has an important effect on both the early "spike" phase and the second, power-law decay phase in the "biphasic" FPTD. Of particular interest here is that, for networks with shorter filaments, the power-law tail of the distribution is wider, meaning the second phase is maintained for longer. Thus a filament network can contribute to both the early-time fast release and upon subsequent shortening also allow the CTRW process to provide a sustained release phase. It is worth noting here that short actin fragments may indeed contribute significantly to the trapping, and hence complete depolymerization (i.e., conversion to G-actin) can have the effect of abolishing CTRW resulting in a comparatively fast release that is not sustained. This is consistent with the fact that glucose stimulation does not alter the F-actin to G-actin ratio and results only in shortening and reorganization [38].

Finally, we showed that, in the presence of a anomalously subdiffusive bulk phase, network-to-network variation in transport times is less significant than cargo-to-cargo transport variation over a single network. This suggests that fine-tuned control of the network geometry (to avoid particularly poorly oriented networks) may not be as important in the presence of anomalous subdiffusion in the bulk. While transport as a whole is slower with a higher variance (which can be functional, as in a sustained release), it may be advantageous for the cell in that it may be easier to control quantities such as the filament length and number using regulatory proteins [44,45] than it would be to control filament network arrangements in geometries that limit variation in cargo transport. Taken together, our results suggest that the coupling between superdiffusive and subdiffusive transport modes allow for filament morphology to be used as a control knob to tune transport dynamics *in vivo*.

ACKNOWLEDGMENTS

This work was supported by National Science Foundation Grant NSF-DMS-1616926. A.G. and B.M. were also partially supported by the NSF-CREST: Center for Cellular and Biomolecular Machines at UC Merced (NSF-HRD-1547848). S.M.A.T. would like to acknowledge the UNI Office of the Provost Pre-tenure Grant, the UNI Graduate College Summer Fellowship, and the UNI College of Humanities, Arts and Sciences Faculty Research Grant. A.G. would also like to acknowledge the hospitality of the Aspen Center for Physics, which is supported by National Science Foundation Grant PHY-1607611, where some of this work was done.

[1] J. L. Ross, M. Y. Ali, and D. M. Warshaw, Cargo transport: Molecular motors navigate a complex cytoskeleton, Curr. Opin. Cell Biol. **20**, 41 (2008).

[2] P. C. Bressloff and J. M. Newby, Stochastic models of intracellular transport, Rev. Mod. Phys. **85**, 135 (2013).

[3] D. Arcizet, B. Meier, E. Sackmann, J. O. Rädler, and D. Heinrich, Temporal Analysis of Active and Passive Transport in Living Cells, Phys. Rev. Lett. **101**, 248103 (2008).

[4] S. M. Ali Tabei, S. Burov, H. Y. Kim, A. Kuznetov, T. Huynh, J. Jureller, L. H. Philipson, A. R. Dinner, and N. F. Sherer, Intracellular transport of insulin granules is a subordinated random walk, Proc. Natl. Acad. Sci. USA **110**, 4911 (2013).

[5] W. M. Saxton and P. J. Hollenbeck, The axonal transport of mitochondria, J. Cell Sci. **125**, 2095 (2012).

[6] J. Howard, *Mechanics of Motor Proteins and the Cytoskeleton* (Sinauer Associates, Sunderland, Massachussetts, 2001).

[7] Z. Wang, S. Khan, and M. P. Sheetz, Single cytoplasmic dynein molecule movements: Characterization and comparison with kinesin, Biophys. J. **69**, 2011 (1995).

[8] A. L. Wells, A. W. Lin, L. Q. Chen, D. Safer, S. M. Cain, T. Hasson, B. O. Carragher, R. A. Milligan, and H. L. Sweeney, Myosin VI is an actin-based motor that moves backwards, Nature (London) **401**, 505 (1999).

[9] G. M. Langford, Actin- and microtubule-dependent organelle motors: Interrelationships between the two motility systems, Curr. Opin. Cell Biol. **7**, 82 (1995).

[10] J. Helenius, G. Brouhard, Y. Kalaidzidis, S. Diez, and J. Howard, The depolymerizing kinesin MCAK uses lattic diffusion to rapidly target microtubule ends, Nature (London) **441**, 115 (2006).

[11] R. Mallik and S. P. Gross, Molecular motors: Strategies to get along, Curr. Biol. **14**, R971 (2004).

[12] S. Klumpp, T. M. Nieuwenhuizen, and R. Lipowsky, Movements of molecular motors: Ratchets, random walks and traffic phenomena, Physica E **29**, 380 (2005).

[13] S. Klumpp and R. Lipowsky, Cooperative cargo transport by several molecular motors, Proc. Natl. Acad. Sci. USA **102**, 17284 (2005).

[14] M. J. I. Müller, S. Klumpp, and R. Lipowsky, Tug-of-war as a cooperative mechanism for bidirectional cargo transport by molecular motors, Proc. Natl. Acad. Sci. USA **105**, 4609 (2008).

[15] A. G. Hendricks, E. Perlson, J. L. Ross, H. W. Schroeder III, M. Tokito, and E. L. F. Holzbaur, Motor coordination via tug-of-war mechanism drives bidirectional vesicle transport, Curr. Biol. **20**, 697 (2010).

[16] D. Ando, M. K. Mattson, J. Xu, and A. Gopinathan, Cooperative protofilament switching emerges from inter-motor interference in multiple-motor transport, Sci. Rep. **4**, 7255 (2014).

[17] K. C. Huang, C. Vega, and A. Gopinathan, Conformational changes, diffusion and collective behavior in monomeric kinesin-based motility, J. Phys.: Condens. Matter **23**, 374106 (2011).

[18] W. H. Liang, Q. Li, K. M. R. Faysal, S. J. King, A. Gopinathan, and J. Xu, Microtubule defects influence kinesin-based transport in vitro, Biophys. J. **110**, 2229 (2016).

[19] S. Klumpp and R. Lipowsky, Asymmetric simple exclusion processes with diffusive bottlenecks, Phys. Rev. E **70**, 066104 (2004).

[20] I. A. Telley, P. Bieling, and T. Surrey, Obstacles on the microtubule reduce the processivity of kinesin-1 in a minimal in vitro system and in cell extract, Biophys. J. **96**, 3341 (2009).

[21] M. W. Gramlich, L. Conway, W. H. Liang, J. A. Labastide, S. J. King, J. Xu, and J. L. Ross, Single molecule investigation of kinesin-1 motility using engineered microtubule defects, Sci. Rep. **7**, 44290 (2017).

[22] D. Ando, N. Korabel, K. C. Huang, and A. Gopinathan, Cytoskeletal network morphology regulates intracellular transport dynamics, Biophys. J. **109**, 1574 (2015).

[23] A. E. Hafner and H. Rieger, Spatial organization of the cytoskeleton enhances cargo delivery to specific target areas on the plasma membrane of spherical cells, Phys. Biol. **13**, 066003 (2016).

[24] A. E. Hafner and H. Rieger, Spatial cytoskeleton organization supports targeted intracellular transport, Biophys. J. **114**, 1420 (2018).

[25] A. Iniguez and J. Allard, Spatial pattern formation in microtubule post-translational modifications and the tight localization of motor-driven cargo, J. Math. Biol. **74**, 1059 (2017).

[26] L. Conway, M. W. Gramlich, S. M. Ali Tabei, and J. L. Ross, Microtubule orientation and spacing within bundles is critical for long-range kinesin-1 motility, Cytoskeleton **71**, 595 (2014).

[27] M. Weiss, Single-particle tracking data reveal anticorrelated fractional Brownian motion in crowded fluids, Phys. Rev. E **88**, 010101(R) (2013).

[28] B. M. Regner, D. Vučinić, C. Domnisoru, T. M. Bartol, M. W. Hetzer, D. M. Tartakovsky, and T. J. Sejnowski, Anomalous diffusion of single particles in cytoplasm, Biophys. J. **104**, 1652 (2013).

[29] B. B. Mandelbrot and J. W. Van Ness, Fractional Brownian motions, fractional noises and applications, SIAM Rev. **10**, 422 (1968).

[30] R. Metzler and J. Klafter, The random walk's guide to anomalous diffusion: A fractional dynamics approach, Phys. Rep. **339**, 1 (2000).

[31] J. H. Jeon, V. Tejedor, S. Burov, E. Barkai, C. Selhuber-Unkel, K. Berg-Sørenson, L. Oddershede, and R. Metzler, In vivo Anomalous Diffusion and Weak Ergodicity Breaking of Lipid Granules, Phys. Rev. Lett. **106**, 048103 (2011).

[32] M. Scholz, S. Burov, K. L. Weirich, B. J. Scholz, S. M. Ali Tabei, M. L. Gardel, and A. R. Dinner, Cycling State that can

Lead to Glassy Dynamics in Intracellular Transport, Phys. Rev. X **6**, 011037 (2016).

[33] A. Caspi, R. Granek, and M. Elbaum, Diffusion and directed motion in cellular transport, Phys. Rev. E **66**, 011916 (2002).

[34] M. Dawson, D. Wirtz, and J. Hanes, Enhanced viscoelasticity of human cystic fibrotic sputum correlates with increasing microheterogeneity in particle transport, J. Biol. Chem. **278**, 50393 (2003).

[35] S. S. Mogre and E. F. Koslover, Multimodal transport and dispersion of organelles in narrow tubular cells, Phys. Rev. E **97**, 042402 (2018).

[36] S. Dey, K. Ching, and M. Das, Active and passive transport of cargo in a corrugated channel: A lattice model study, J. Chem. Phys. **148**, 134907 (2018).

[37] J. Beeg, S. Klumpp, R. Dimova, R. S. Garcia, and E. Unger, Transport of beads by several kinesin motors, Biophys. J. **94**, 532 (2008).

[38] Z. Wang and D. C. Thurmond, Mechanisms of biphasic insulin-granule exocytosis—Roles of the cytoskeleton, small GTPases and SNARE proteins, J. Cell Sci. **122**, 893 (2009).

[39] See Supplemental Material at http://link.aps.org/supplemental/10.1103/PhysRevE.99.062404 for discussion of system size effects, parameter values, simulation details, and pseudocode.

[40] Y. He, S. Burov, R. Metzler, and E. Barkai, Random Rime-Scale Invariant Diffusion and Transport Coefficients, Phys. Rev. Lett. **101**, 058101 (2008).

[41] R. T. Watson and J. E. Pessin, Glut4 translocation: The last 200 nanometers, Cell. Signal. **19**, 2209 (2007).

[42] A. Tomas, B. Yermen, L. Min, J. E. Pessin, and P. A. Halban, Regulation of pancreatic β-cell insulin secretion by actin cytoskeleton remodelling: Role of gelsolin and cooperation with the MAPK signalling pathway, J. Cell Sci. **119**, 2156 (2006).

[43] M. A. Kalwat and D. C. Thurmond, Signaling mechanisms of glucose-induced f-actin remodeling in pancreatic islet β cells, Exp. Mol. Med. **45**, e37 (2013).

[44] A. Gopinathan, K. C. Lee, J. M. Schwarz, and A. J. Liu, Branching, Capping, and Severing in Dynamic Actin Structures, Phys. Rev. Lett. **99**, 058103 (2007).

[45] A. E. Carlsson, Structure of Autocatalytically Branched Actin Solutions, Phys. Rev. Lett. **92**, 238102 (2004).